Systems biophysics: Global and target analysis of light harvesting and photochemical quenching in vivo

van Stokkum, Ivo

published in
Light Harvesting in Photosynthesis
2018

document version
Publisher's PDF, also known as Version of record

citation for published version (APA)
van Stokkum, I. (2018). Systems biophysics: Global and target analysis of light harvesting and photochemical quenching in vivo. In R. Croce, R. van Grondelle, H. van Amerongen, & I. van Stokkum (Eds.), *Light Harvesting in Photosynthesis* (pp. 467-482). CRC Press, Boca Rata.

20

Systems biophysics: Global and target analysis of light harvesting and photochemical quenching *in vivo*

IVO VAN STOKKUM

ABBREVIATIONS

Chl	Chlorophyll
DAS	Decay-Associated Spectrum
EAS	Evolution-Associated Spectrum
EET	excitation energy transfer
FWHM	full width at half maximum
IRF	instrument response function
LHC	light-harvesting complex
MA	magic angle
$n\lambda$	number of wavelengths
nt	number of time points
PS	photosystem
RC	reaction center
SAS	Species-Associated Spectrum
SVD	singular value decomposition
TCSPT	time-correlated single photon timing

20.1 SUMMARY

Systems biophysics can describe the input to a photosynthetic system and thus contribute a building block to the systems biology of photosynthesis. Systems biophysics mathematically describes the processes during the light reactions of photosynthesis: light harvesting, energy transfer, photochemical quenching (charge separation), nonphotochemical quenching, and state transitions. The aim of *systems biophysics* is to develop

mathematical models that describe the functioning of complex photosynthetic systems. Such models are based upon measured time-resolved absorption and emission spectra, which are two-dimensional data sets. Theoretical methods and software have been developed to identify the model and estimate the biophysical parameters that describe all data. These methods are termed global and target analysis. Key ingredients are compartmental, spectral, and thermodynamic models. The methods will be demonstrated with case studies of cyanobacterial light harvesting and photochemical quenching *in vivo*.

20.2 INTRODUCTION

Systems theory methods are widely used in biophysics to describe the functioning of systems with the help of mathematical models. Light absorbed by a light-harvesting complex provides the input to a photosynthetic system, for example, the thylakoid membrane. The final outputs of the thylakoid membrane are energized molecules: reduction equivalents (NADPH) and ATP. This chapter will be limited to light harvesting, energy transfer, and photochemical quenching (charge separation) in photosystems (van Grondelle et al. 1994; Croce and van Amerongen 2013; van Amerongen and Croce 2013).

Cyanobacteria are model systems for studies of photosynthesis. They can be mutated, which allows us to study the properties of subsystems *in vivo*. In particular, the BE and PAL mutant of *Synechocystis* (Ajlani and Vernotte 1998; Krumova et al. 2010; Tian et al. 2013) can be considered elementary photosynthetic systems. They lack the phycobilisome antenna. The BE mutant only contains photosystem I (PSI) complexes, whereas the PAL mutant contains both PSI and photosystem II (PSII) complexes.

Time-resolved spectroscopy has proven to be extremely useful in photosynthesis research in the past decades. Both absorption and emission spectroscopy have been employed in a variety of wavelength ranges. When the superposition principle applies, the system can be considered linear. After excitation by a short laser flash, the (excited state) dynamics of the system can be studied by measuring a time-resolved spectrum. In the language of linear systems theory, the time-resolved spectrum can be considered the response of the system, which is a convolution of the impulse response (the response after a unit impulse of negligible width) and the instrument response function (IRF) (van Stokkum et al. 2004).

This chapter will be limited to measurements of chlorophyll *a* (Chl *a*) emission from PSI or PSII at magic angle. For analysis of polarized light experiments where anisotropy comes into play and for transient absorption experiments the reader is referred to van Stokkum et al. (2004). Time-resolved emission spectra can be measured with low excitation intensities, thus avoiding nonlinear effects like annihilation, which can be problematic with transient absorption experiments (Muller et al. 1996).

20.3 FIRST DATA: THE TIME-RESOLVED EMISSION SPECTRUM OF BE CELLS

To monitor the fluorescence, a synchroscan streak camera in combination with a spectrograph is employed. It can simultaneously record the temporal dynamics and wavelength of fluorescence representable as an image with time and wavelength along the axes (van Stokkum et al. 2008). The time-resolved spectrum of BE cells at room temperature after 400 nm excitation is depicted in Figure 20.1. The emission evolves both temporally and spectrally: it rises due to the finite rise time of the instrument; the spectral shape evolves due to the equilibration between Chl pigments with different properties; and finally, it decays due to photochemical quenching (charge separation, trapping) in the reaction center (RC) (Gobets et al. 2001).

20.3.1 Usage of the singular value decomposition

The matrix structure of the streak data enables the usage of matrix decomposition techniques, in particular, the singular value decomposition (SVD) (Shrager 1986; Henry and Hofrichter 1992; Hendler and Shrager 1994). Formally, the data matrix can be decomposed as (Golub and Van Loan 1996)

$$\psi(t,\lambda)=\sum_{l=1}^{m}u_l(t)s_l w_l(\lambda)$$

where

- u_l and w_l are the left and right singular vectors
- s_l is the sorted singular value
- m is the minimum of the number of rows and columns of the data matrix

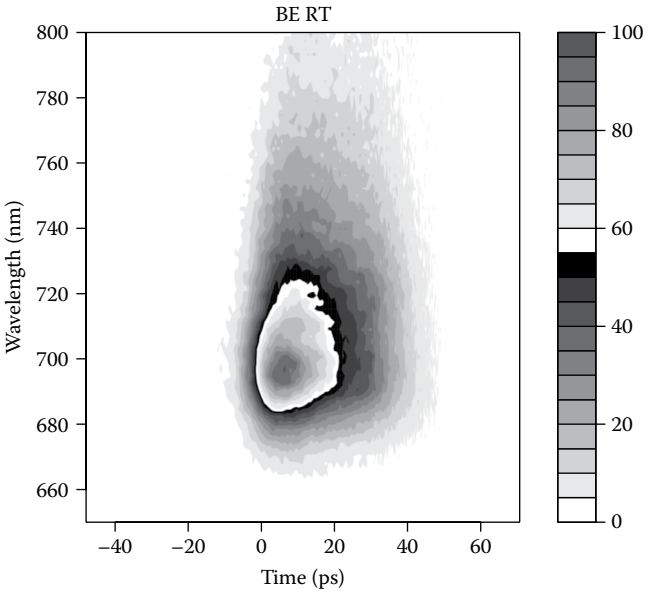

Figure 20.1 Filled contour plot of the time-resolved emission spectrum of BE cells (containing only PSI) at room temperature after 400 nm excitation. Time step ≈ 0.8 ps, wavelength step ≈ 2 nm.

The singular vectors are orthogonal and provide an optimal least squares approximation of the matrix. From the SVD, the rank of the data matrix can be estimated, as judged from the singular values and singular vector pairs significantly different from noise. This rank corresponds to the number of spectrally and temporally independent components n_{comp}. When the data matrix has not been corrected for dispersion, this is no longer strictly true, and then the singular values provide only an indication of n_{comp}. Furthermore, the SVD of the matrix of residuals is useful to diagnose shortcomings of the model used, or systematic errors in the data.

Figure 20.2a through c depicts the SVD of the PSI data, where three singular values and singular vector pairs are significantly different from noise. These first three singular values account for 96.5% of the variance of the data matrix. The left and right singular vectors are both linear combinations of the true concentration profiles and SAS and are hard to interpret. The first pair (squares) represents a kind of average. The SVD of the residual matrix will be discussed later.

20.4 GLOBAL AND TARGET ANALYSIS

The aim of global data analysis in general is to obtain a model-based description of the *full* data set in terms of a model containing a small number of precisely estimated parameters. Our main assumption here is that the time and wavelength properties of the system of interest are *separable*, which means that the spectra of species or states are independent of time. Analogously, the dynamics of species or states are assumed to be wavelength independent. When applicable, a wavelength dependence of the IRF location can be described parametrically (see Section 20.4.1). Thus, the adjective *global* (Beechem et al. 1985; Beechem 1989) indicates that the kinetic and spectral parameters of the model apply to the *full* data set. The adjective *target* (Arcioni and Zannoni 1984) refers to the targeted model.

A description of the basic ingredient of kinetic models, the exponential decay, will be given first, followed by a description of how to use these ingredients for global and target analysis (see, e.g., the reviews by Holzwarth (1996) and van Stokkum et al. (2004)) of the full data. The parameter estimation is generally based on nonlinear least squares. Because of the wealth of conditionally linear parameters, the variable projection algorithm is crucial (Golub and Pereyra 1973, 2003; Golub and LeVeque 1979; Nagle 1991; Mullen and van Stokkum 2009). For further details on parameter estimation techniques, the reader is also referred to the previously cited reviews and references cited therein and to van Stokkum (2005). Software

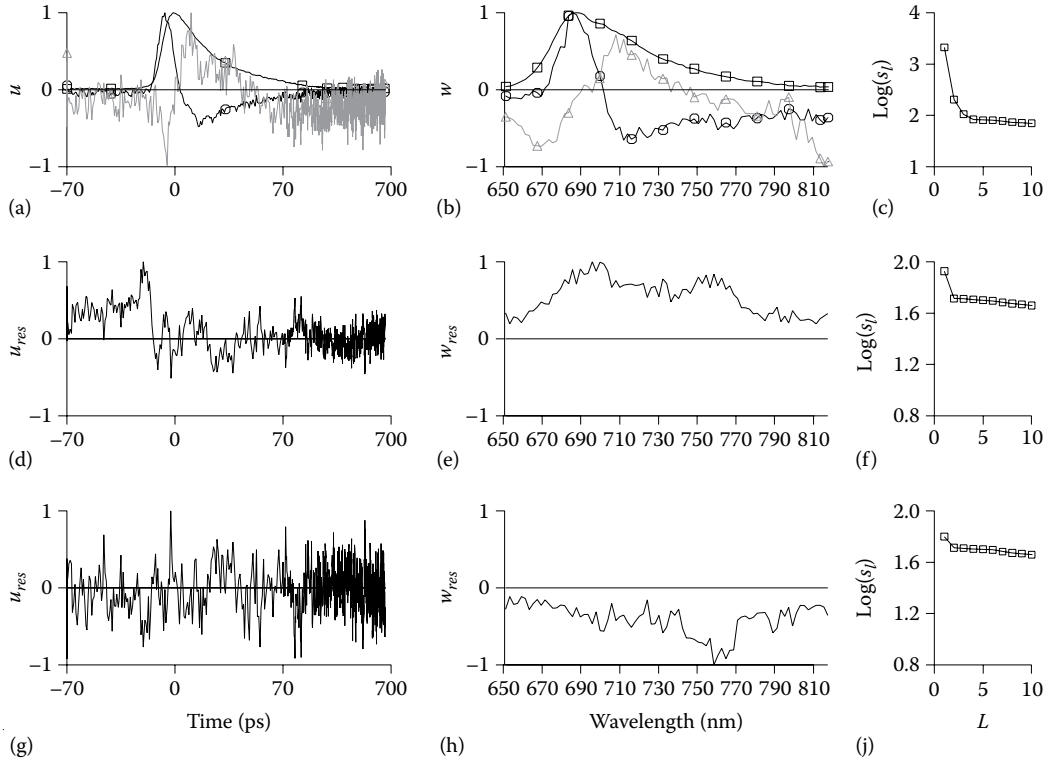

Figure 20.2 SVD of the PSI data matrix **(a–c)** and matrix of residuals **(d–i)**. **(a)** First 3 (order squares, circles, triangles) left singular vectors u_l, (b) first 3 right singular vectors w_l, **(c)** first 10 singular values s_l on a logarithmic scale. Panels **(d–f)** represent the matrix of residuals from a fit using a simple Gaussian IRF: the first left singular vector $u_{res,1}$, the first right singular vector $w_{res,1}$, and the first 10 singular values $s_{res,l}$ on a logarithmic scale. Panels **(g–i)** represent the matrix of residuals from a fit using a triple Gaussian IRF. Further explanation in text.

issues are discussed in Snellenburg et al. (2012); van Stokkum and Bal (2006); Mullen and van Stokkum (2007).

20.4.1 Modeling an exponential decay

Here, an expression is derived for describing the contribution of an exponentially decaying component to the streak image. The IRF $i(t)$ can usually adequately be modeled with a Gaussian with parameters μ and Δ for, respectively, location and full width at half maximum (FWHM):

$$i(t) = \frac{1}{\tilde{\Delta}\sqrt{2\pi}} \exp\left(-\log(2)\left(2(t-\mu)/\Delta\right)^2\right)$$

where $\tilde{\Delta} = \Delta / \left(2\sqrt{2\log(2)}\right)$. The adequacy of the Gaussian approximation of the IRF shape is depicted in Figure 20.3a of van Stokkum et al. (2008). The convolution (indicated by an $*$) of this IRF with an exponential decay (with rate k) yields an analytical expression, which facilitates the estimation of the IRF parameters μ and Δ:

$$c(t, k, \mu, \Delta) = \exp(-kt) * i(t)$$

$$= \frac{1}{2}\exp(-kt)\exp\left(k\left(\mu + \frac{k\tilde{\Delta}^2}{2}\right)\right)$$

$$\times\left\{1 + \operatorname{erf}\left(\frac{t - \left(\mu + k\tilde{\Delta}^2\right)}{\sqrt{2}\tilde{\Delta}}\right)\right\}$$

The periodicity of the synchroscan results in the detection of the fluorescence that remains after multiples of half the synchroscan period T (typically $T \approx 13$ ns). Therefore, if lifetimes longer than ≈1 ns occur in a sample, the said expression

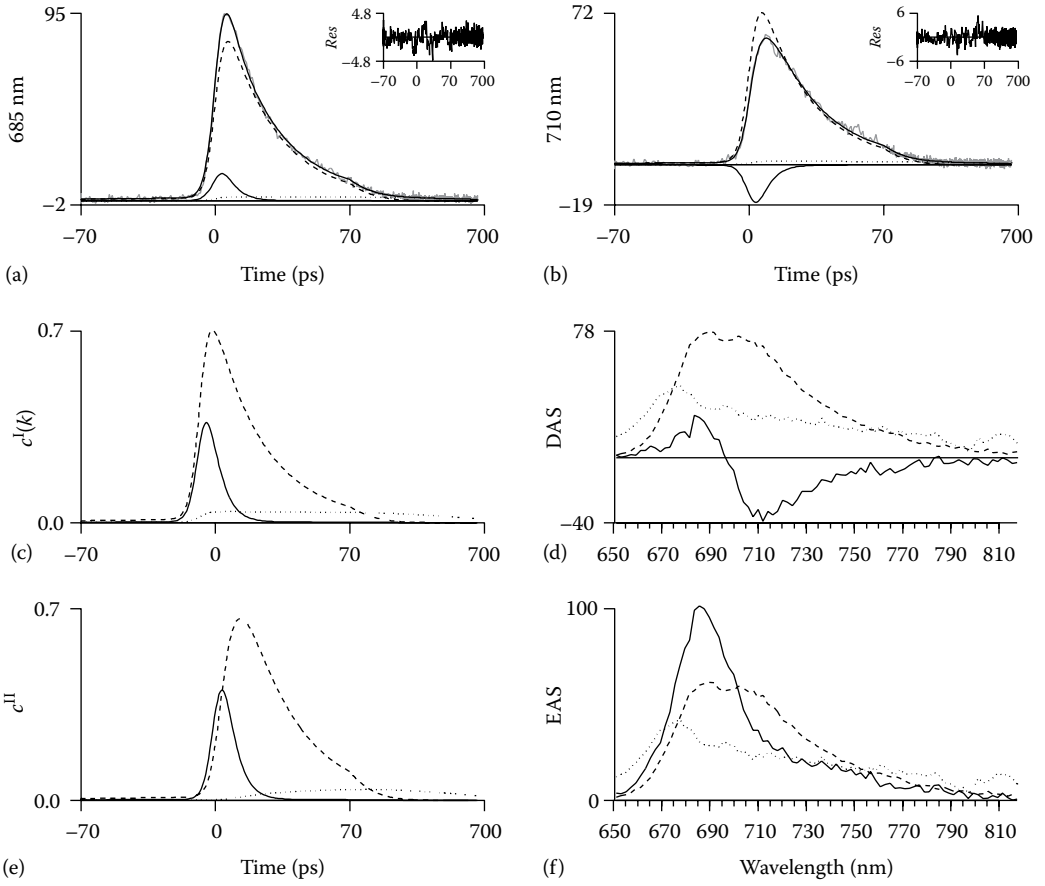

Figure 20.3 Results from global analysis of BE mutant (PSI) data depicted in Figure 20.1. Note that in a–c and e, the time axis is linear from –70 to +70 ps relative to the maximum of the IRF and logarithmic thereafter. Insets in a and b show residuals. **(a)** Data (in grey) and fit (in black) of 685 nm emission trace showing multiexponential decay. Contributions of the three exponential decays with different lifetimes (shown in c) multiplied by their amplitudes at 685 or 710 nm (shown in d) are indicated by line type in panels a and b. **(b)** Data (in grey) and fit (in black) of 710 nm emission trace showing multiexponential rise (visible as a contribution of $c^{I}(k_1)$ with negative amplitude) and decay. **(c)** Exponential decays $c^{I}(k_i)$. Estimated lifetimes (in panels c and e): 5.8 ps (solid), 26.4 ps (dashed), 0.59 ns (dotted). Note that in panels c and e, the dotted concentration profile was divided by 25. **(d)** Estimated Decay-Associated Spectra (DAS). Note that in panels d and f, the dotted spectrum was multiplied by 25 to increase its visibility. **(e)** Evolutionary concentration profiles c_i^{II} (assuming a sequential kinetic scheme with increasing lifetimes). **(f)** Estimated Evolution-Associated Spectra (EAS).

should be extended with a summation over the signal contributions that result from forward and backward sweeps:

$$c(t,k,T)=\sum_{n=0}^{\infty}e^{-kTn}\left\{e^{-k(t-\mu+T)}+e^{-k(T/2-t-\mu)}\right\}$$

$$=\frac{\left\{e^{-k(t-\mu+T)}+e^{-k(T/2-t-\mu)}\right\}}{\left(1-e^{-kT}\right)}$$

Note that it is assumed here that time zero of the time base corresponds to the zero crossing of the sweep and that the convolution with the IRF is no longer necessary at times longer than $T/2$. Adding the previous expressions provides the full model function for an exponential decay recorded with a synchroscan streak camera and will henceforth be denoted by $c^{I}(k)$:

$$c^{I}(k)\equiv c(t,k,\mu,\Delta,T)=c(t,k,\mu,\Delta)+c(t,k,T)$$

Because fluorescence samples are relatively dilute, elastic scattering or Raman scattering of the excitation light by water (or of other solvents) can complicate the measurement if they occur within the analyzed wavelength interval. Such contributions can be modeled with an extra component with a time course identical to the IRF $i(t)$. Usually, it is possible to restrict the contribution of scattering to a limited wavelength region.

If the streak image has not been corrected for the instrumental curvature, the wavelength dependence of the IRF location μ can be modeled with a polynomial (usually a parabola is adequate). Sometimes, the IRF shape is better described by a superposition of two or even three Gaussians (with common location μ), leading to a superposition description of the exponential decay (van Stokkum, 2005). We will return to this later.

The IRF description given earlier for the synchroscan streak camera is fairly complicated. With time-resolved absorption spectroscopy, the Gaussian approximation of the IRF shape describes the pump-probe overlap rather well. With time-correlated single photon timing (TCSPT) the IRF can be measured via scatter (at the excitation wavelength) or with a fast-decaying reference compound (at the detection wavelength). In practice, the TCSPT IRF can be well approximated by a superposition of three or four Gaussians (with different locations μ).

20.4.2 The superposition principle

The basis of global analysis is the superposition principle, which states that the measured data $\psi(t,\lambda)$ result from a superposition of the spectral properties $\varepsilon_l(\lambda)$ of the components present in the system of interest weighted by their concentration $c_l(t)$:

$$\psi(t,\lambda) = \sum_{l=1}^{n_{comp}} c_l(t)\varepsilon_l(\lambda)$$

The $c_l(t)$ of all n_{comp} components are described by a compartmental model that consists of first-order differential equations, with sums of exponential decays as solution. We will consider three types of compartmental models: (1) a model with components decaying monoexponentially in parallel, which yields Decay-Associated Spectra (DAS); (2) a sequential model with increasing lifetimes, also called an unbranched unidirectional model, giving rise to Evolution-Associated Spectra (EAS); and (3) a full compartmental scheme, which may include possible branchings and equilibria, yielding Species-Associated Spectra (SAS). The latter is most often referred to as target analysis, where the target is the proposed kinetic scheme, including possible spectral assumptions.

20.4.3 Components decaying in parallel: DAS

With components decaying in parallel, the model reads

$$\psi(t,\lambda) = \sum_{l=1}^{n_{comp}} c^{\mathrm{I}}(k_l)\,DAS_l(\lambda)$$

The DAS thus represent the estimated amplitudes of the defined exponential decays $c^{\mathrm{I}}(k_l)$.

Three components are sufficient to describe the data. The adequacy of the fit is judged from the SVD of the first left and right singular vectors of the matrix of residuals. With a simple Gaussian IRF shape, the residuals (shown in Figure 20.2d through f) show some structure, especially at times before the maximum of the IRF, and at all wavelengths where there is signal. This indicates that the IRF shape is more complicated. Therefore, we applied a triple Gaussian IRF shape with FWHM 9 ps (61% of the area), 15 ps (29%), and 204 ps (10%). We attribute these small fractions of wider IRF to shortcomings of the synchroscan. The trends are no longer present in Figure 20.2g and h. The rms error of the fit decreased from 1.154 to 1.136, which is just over 1% of the peak in Figure 20.1.

The estimated lifetimes (reciprocals of estimated rate constants k_l) are 5.8 ± 0.2 ps, 26.4 ± 0.2 ps, and 0.59 ± 0.02 ns.

The estimated DAS from the PSI data are shown in Figure 20.3d. Several observations can be made: the 5.8 ps DAS (solid) is nearly conservative, that is, the positive and negative areas are almost equal. It represents decay of more blue and rise of more red emission and can be interpreted as energy transfer from Bulk to Red Chl *a*, that is, Chl *a* that absorbs at wavelengths longer than the primary electron donor P700. Thus, *in vivo*, the excited state equilibration time constant of PSI is 5.8 ps (Krumova et al. 2010; Chukhutsina et al. 2013). The 26.4 ps DAS represents the trapping spectrum. The long-lived (0.59 ns) DAS

(dotted) was multiplied by 25 to increase its visibility. It has a maximum near 670 nm and resembles the shape of a Chl *a* fluorescence spectrum. Most probably it is not connected to PSI. It could be the single Chl *a* present in cytochrome b6f (Peterman et al. 1998). Henceforth, it will be referred to as "free" Chl *a*. Note that in a steady-state spectrum its contribution will be as large as that of PSI, because of its long lifetime. Clearly, the first two DAS do not represent pure species, and they are interpreted as linear combinations (with positive and negative contributions) of true species spectra.

Note that the ultrafast (≪1 ps) rise due to the relaxation from the initially excited Soret state (higher excited state, of which the ≈460 nm emission is outside the detection range) to the Q_y emission (lowest excited state) cannot be resolved in this experiment due to the limited time resolution (the main FWHM Δ of the IRF was 9 ps).

20.4.4 Sequentially decaying components: EAS

The sequential model reads

$$\psi(t,\lambda) = \sum_{l=1}^{n_{comp}} c_l^{\mathrm{II}} EAS_l(\lambda)$$

where each concentration is a linear combination of the exponential decays (Nagle et al. 1982), $c_l^{\mathrm{II}} = \sum_{j=1}^{l} b_{jl} c^I(k_l)$, and the amplitudes b_{jl} are given by $b_{11} = 1$ and for $j \le l$:

$$b_{jl} = \frac{\prod_{m=1}^{l-1} k_m}{\prod_{n=1, n\neq j}^{l} (k_n - k_j)}$$

Examples of c_l^{II} are depicted in Figure 20.3e, whereas the estimated EAS are shown in Figure 20.3f. With increasing lifetimes and thus decreasing rates k_l, the first EAS (equal to the sum of DAS) corresponds to the spectrum at time zero with an ideal infinitely small IRF, $i(t) = \delta(t)$. The first EAS (solid line in Figure 20.3f) represents the sum of the spectra of all excitations that have arrived from the Soret region and is dominated by Bulk Chl *a*. The second EAS, which is formed with a time constant of 5.8 ps and decays with a time constant of 26.4 ps, contains more Red Chl *a* emission and represents a Boltzmann equilibrium of all PSI Chl *a* pigments. In this interpretation, we neglect the small contribution of the long-lived (0.59 ns) "free Chl *a*." When we collate the concentration profiles of the parallel and sequential model in matrices C^{I} and C^{II}, with *nt* rows and n_{comp} columns, respectively, these obey the matrix relation $C^{\mathrm{II}} = C^{\mathrm{I}} B$, with the elements of the $n_{comp} \times n_{comp}$ upper triangular *B* matrix defined earlier. Likewise, we form $n\lambda \times n_{comp}$ matrices DAS and EAS that contain the DAS_l and EAS_l of the components. In matrix form, the superposition model for the $nt \times n\lambda$ data matrix Ψ is expressed as $\Psi = C^{\mathrm{I}} \cdot DAS^T$ (parallel) or $\Psi = C^{\mathrm{II}} \cdot EAS^T$ (sequential). In global analysis (without any spectral constraints, see Section 20.4.5), the parallel and sequential model result in *exactly* the same residuals and *exactly* the same estimated lifetimes. The estimated concentration profiles obey $C^{\mathrm{II}} = C^{\mathrm{I}} B$, and therefore the estimated DAS and EAS are related as $C^{\mathrm{II}} \cdot EAS^T = C^{\mathrm{I}} B \cdot EAS^T = C^{\mathrm{I}} \cdot DAS^T$, which leads to $B \cdot EAS^T = DAS^T$ or when transposed, $EAS \cdot B^T = DAS$ or $EAS = DAS \cdot B^{-T}$. The lower triangular matrix B^T can be inverted, yielding $b_{1l}^{-1} = 1 = b_{l1}^{-T}$ and

$$b_{jl}^{-1} = \prod_{n=1}^{j-1} \frac{(k_n - k_l)}{k_n} = b_{lj}^{-T}$$

For the three components of the global analysis, we can compute (inserting $k_1 = 0.173$, $k_2 = 0.038$, $k_3 = 0.0016$)

$$B = \begin{bmatrix} 1 & -k_1/(k_1-k_2) & k_1/(k_1-k_2)\cdot k_2/(k_1-k_3) \\ 0 & k_1/(k_1-k_2) & k_1/(k_1-k_2)\cdot k_2/(k_3-k_2) \\ 0 & 0 & k_1/(k_1-k_3)\cdot k_2/(k_2-k_3) \end{bmatrix}$$

$$= \begin{bmatrix} 1 & -1.28 & 0.28 \\ 0 & 1.28 & -1.34 \\ 0 & 0 & 1.06 \end{bmatrix}$$

$$B^{-T} = \begin{bmatrix} 1 & 0 & 0 \\ 1 & (k_1-k_2)/k_1 & 0 \\ 1 & (k_1-k_3)/k_1 & (k_1-k_3)/k_1 \cdot (k_2-k_3)/k_2 \end{bmatrix}$$

$$= \begin{bmatrix} 1 & 0 & 0 \\ 1 & 0.78 & 0 \\ 1 & 0.99 & 0.95 \end{bmatrix}$$

This leads to the following relations for the DAS_l and EAS_l of the components:

$$EAS_1 = DAS_1 + DAS_2 + DAS_3$$

$$EAS_2 = 0.78DAS_2 + 0.99DAS_3$$

$$EAS_3 = 0.95DAS_3$$

$$DAS_1 = EAS_1 - 1.28EAS_2 + 0.28EAS_3$$

$$DAS_2 = 1.28EAS_2 - 1.34EAS_3$$

20.4.5 Target model: SAS

When neither of these two simple models is applicable, a full kinetic scheme may be appropriate. This is called a compartmental model. The problem with most kinetic schemes is that while the kinetics are described by more than n_{comp} microscopic rate constants (due to branchings or equilibria), the data only allows for the estimation of n_{comp} decay rates (or lifetimes). Then additional information is required to estimate the microscopic rates (Nagle 1991), which can be spectral constraints (zero contribution of SAS at certain wavelengths) or spectral relations. This is detailed in van Stokkum et al. (2004).

Now the model reads

$$\psi(t,\lambda) = \sum_{l=1}^{n_{comp}} c_l^{\mathrm{III}} SAS_l(\lambda)$$

Disregarding the small contribution of the long-lived (0.59 ns) "free Chl *a*," we can describe the PSI dynamics by the following two coupled differential equations (omitting the superscript III):

$$\frac{d}{dt}\begin{bmatrix} c_1(t) \\ c_2(t) \end{bmatrix} = \begin{bmatrix} -(k_{01}-k_{21}) & k_{12} \\ k_{21} & -(k_{02}-k_{12}) \end{bmatrix}\begin{bmatrix} c_1(t) \\ c_2(t) \end{bmatrix} + \begin{bmatrix} x_1 \\ x_2 \end{bmatrix} i(t)$$

where the indices 1 and 2 refer to Bulk and Red Chl *a*, respectively. It is known that a PSI monomer contains about six Red Chl *a* and 90 Bulk Chl *a*; thus, the inputs to the system are $x_1 = 90/96$ and $x_2 = 6/96$. There are four microscopic rate constants, k_{21} and k_{12} representing the equilibration, k_{01} representing the photochemical quenching (trapping), and k_{02} representing the natural lifetime (k_f) of a Chl *a*. Typically, $k_f \approx 1/(2ns)$, but this means that still three microscopic rate constants need to be estimated, whereas only two lifetimes and two SAS_l can be estimated. Thus, spectral constraints imposed on the two SAS_l are needed. When modeling emission data, a natural spectral constraint is nonnegativity of the SAS_l (Mullen and van Stokkum 2009). However, this constraint is still not enough. A strong spectral constraint is $SAS_2 = 0$ in an appropriate wavelength range (typically below 685 nm for Red Chl *a*). This strong constraint is enough to estimate the equilibrium between the two states (Muller et al. 1992; Gobets et al. 2001). A mild spectral constraint is to assume that the area under the SAS_l is equal for states of equal oscillator strength like Bulk and Red Chl *a* (Snellenburg et al. 2013). This mild constraint is also enough to estimate the equilibrium between the two states and is especially useful when a strong zero constraint cannot be applied. Formally, when the ratio between the oscillator strengths of two Chl species with SAS_i and SAS_j is assumed to be α, a penalty can be imposed, which is added to the least squares criterion of the fit:

$$\text{penalty}_{ij} = \text{weight}_{ij} \int_{\lambda\min}^{\lambda\max} \left| SAS_i(\lambda) - \alpha SAS_j(\lambda) \right| d\lambda$$

Without *a priori* knowledge, we assume that all Chl species possess the same oscillator strength, that is, $\alpha = 1$. Here, weight_{ij} is used to tune the importance of this area constraint in the least squares fitting process.

20.4.5.1 SOLVING THE COMPARTMENTAL MODEL

The general compartmental model with p compartments can be abbreviated as $\frac{d}{dt}c(t) = Kc(t) + j(t)$ with $c(t) = \left[c_1(t) \ldots c_p(t)\right]^T$, $j(t) = i(t)x$; $x = \left[x_1 \ldots x_p\right]^T$ is a vector that describes the amount of excitation of each compartment. In this example, the concentration vector is $c(t) = \left[c_1(t) \quad c_2(t)\right]^T$ and the input vector is $j(t) = i(t)\left[x_1 \quad x_2\right]^T$. The transfer matrix K contains off-diagonal elements k_{ij}, representing the microscopic rate constant from compartment j to compartment i. k_{0j} indicates decay from compartment j to the outside of the system described.

The diagonal elements contain the total decay rates of each compartment. To solve a compartmental model, we employ the eigendecomposition of K given by $U\Lambda U^{-1}$ with $\Lambda = diag(-\kappa_1, -\kappa_2, \ldots, -\kappa_p)$, the diagonal matrix containing the eigenvalues $-\kappa_l$ of K, and U, the matrix with the eigenvectors as columns (check: $KU = U\Lambda U^{-1}U = U\Lambda$, thus each eigenvector is scaled by its eigenvalue). Thus, we have $e^{Kt} = Ue^{\Lambda t}U^{-1}$ $\left(\text{since } \exp(Kt) = \sum_{n=0}^{\infty}(Kt)^n/n! \text{ and } K^n = U\Lambda U^{-1}\ldots U\Lambda U^{-1} = U\Lambda^n U^{-1}, \text{thus} \sum_{n=0}^{\infty}(Kt)^n/n! = U\left(\sum_{n=0}^{\infty}(Kt)^n/n!\right)U^{-1} = U\exp(\Lambda t)U^{-1}\right)$ and

$$
\begin{aligned}
c^{\mathrm{III}}(t) &= e^{Kt} * j(t) \\
&= U\,\mathrm{diag}\left(U^{-1}x\right)\begin{bmatrix} e^{-\kappa_1 t} * i(t) \\ \ldots \\ e^{-\kappa_p t} * i(t) \end{bmatrix} \\
&= U\,\mathrm{diag}\left(U^{-1}x\right)\begin{bmatrix} c^{\mathrm{I}}(\kappa_1) \\ \ldots \\ c^{\mathrm{I}}(\kappa_p) \end{bmatrix}
\end{aligned}
$$

Thus, the solution of the general compartmental model is a linear combination of $c^{\mathrm{I}}(\kappa_l)$. The concentration of each compartment is a linear combination of at most p exponential decays (convolved with the IRF), with coefficients that depend upon the microscopic rate constants that describe the transitions between all the compartments.

20.4.5.2 DETAILED BALANCE

When two compartments, i and j, are at equilibrium, we have

$$k_{ij}c_j(t) = k_{ji}c_i(t)$$

and we can compute the Gibbs free energy difference between compartments i and j as

$$\Delta G_{ij} = k_B T \ln\left(\frac{k_{ji}}{k_{ij}}\right)$$

For a closed system at equilibrium, the sum of the Gibbs free energy differences of a cycle equals zero. Thus, for example, with three compartments, the product of the clockwise rate constants 1→2→3→1 is equal to the product of the counterclockwise rate constants 1←2←3←1:

$$k_{21}k_{32}k_{13} = k_{12}k_{31}k_{23}$$

This is called a detailed balance condition. It must be fulfilled and reduces the number of unknown microscopic rate constants (Nagle 1991).

20.4.5.3 TARGET ANALYSIS OF THE FIRST DATA

The kinetic scheme used for the target analysis of the BE PSI data is depicted in Figure 20.4a. As explained earlier, three microscopic rates, the forward and backward rate constants between the Bulk (B) and Red (R) Chl *a* compartment and the rate of photochemical quenching from B, were estimated with the help of the mild spectral constraint that the area under the SAS_l is equal for states B and R. The shapes of the estimated SAS shown in Figure 20.4c are realistic. Very small amplitudes of SAS_R are present below 690 nm.

The free energy difference between two compartments depends upon the energy difference between the two emission maxima and upon the relative number of pigments of the compartments ($k_B T \ln(N_1/N_2)$). We estimate the energetic contribution from the difference between the average emission wavelengths of the B and R SAS, 703.6 and 722.7 nm, for B* and R*, respectively. This corresponds to 47 meV. The observed free energy difference is $\Delta G_{12} = k_B T \ln(k_{21}/k_{12}) = k_B T \ln(61/126) = -18$ meV. The entropic free energy difference thus equals 47 + 18 = 65 meV, which is equal to $k_B T \ln(N_1/N_2)$, with N_1 and N_2, the number of pigments in the B and R compartments. Using $k_B T = 25$ meV, we thus find $N_1/N_2 = 13.1$, which is consistent with N_1 and N_2 comprising ≈92 and ≈7 pigments, respectively. This is very close to the assumption that the PSI monomer contains about six Red Chl *a* and 90 Bulk Chl *a*.

The eigenvalues of the K matrix correspond to lifetimes of 4.7 and 28 ps and 0.68 ns. These lifetimes differ slightly from those estimated in the global analysis (5.6 and 26.4 ps and a very small contribution of 0.59 ns). The difference is attributed to the limited signal to noise ratio of the data. Apparently, the relative precision of the estimated lifetimes is typically about 10%. The quality of the fit (indicated by rms errors and

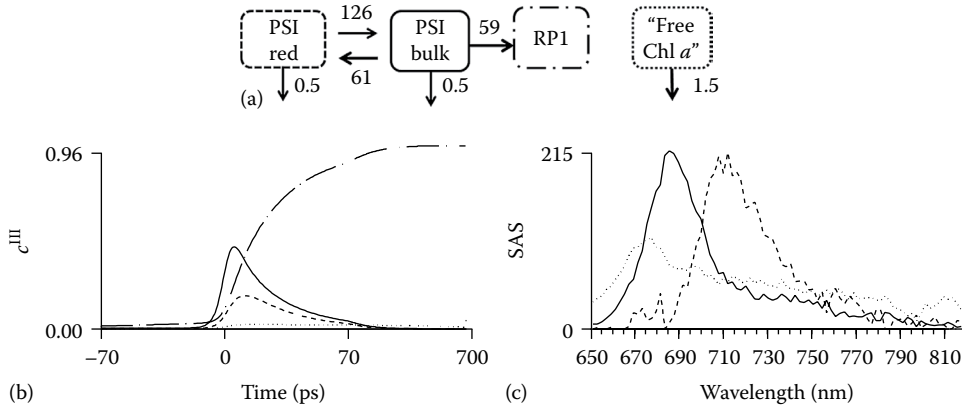

Figure 20.4 **(a)** Kinetic scheme used for the target analysis of the BE PSI data depicted in Figure 20.1. After excitation in the Soret band, three compartments are populated: Bulk Chl *a* (B), Red Chl *a* (R), and a small fraction of "free Chl *a*" (F). The first two compartments equilibrate, and excitations are trapped from B. Rates in 1/ns. **(b)** Concentration profiles c_i^{III}; note that the time axis is linear from –70 to +70 ps relative to the maximum of the IRF and logarithmic thereafter. **(c)** Species-Associated Spectra (SAS). Key in a, b, and c: Bulk Chl *a* (solid), Red Chl *a* (dashed), "free Chl *a*" (dotted). In addition, panel b depicts the rise of the charge-separated state (radical pair) RP1 (reaching 0.96) in dot-dash.

structure of the residual matrix) of the global analysis and of the target analysis are practically the same.

Finally, the amplitude matrix A is presented in Table 20.1, which expresses the relation between the concentration profiles c_i^{III} and the exponential decays $c^I(\kappa_i)$, $C^{III} = A \cdot C^I$.

The interpretation of the amplitude matrix is as follows (neglecting the IRF):

$$c_B = 0.392\exp(-t/4.7) + 0.508\exp(-t/28),$$
$$c_R = -0.282\exp(-t/4.7) + 0.342\exp(-t/28),$$
$$c_{RP1} = -0.110\exp(-t/4.7) - 0.838\exp(-t/28) + 0.948$$

The total PSI excitation is 0.96, and the RP1 yield is 0.948/0.96 = 99%. No attempt is made to resolve the equilibration within the Bulk compartment to and from the RC. Several models are discussed in van Stokkum et al. (2013); Muller et al. (2010).

20.5 SECOND DATA: THE TIME-RESOLVED EMISSION SPECTRUM OF PAL CELLS

The time-resolved spectrum of PAL cells at room temperature after 400 nm excitation is depicted in Figure 20.5. The PSIIRC is in the open state (a) or in the closed state due to the presence of DCMU (b). Note that PAL cells contain both PSI and PSII, and thus a target model must be a superposition of target models for both PSI and PSII.

Again, the emission evolves both temporally and spectrally: it rises due to the finite rise time of the instrument, the spectral shape evolves due to equilibration between Chl pigments with different properties, and finally it decays due to photochemical quenching (charge separation, trapping) in the RCs (PSIRC and PSIIRC).

Table 20.1 Amplitude matrix for the different lifetimes of the BE PSI data

Compartment	Red	Bulk	RP1	F
Excitation	0.06	0.90	0	0.024
4.7 ps	–0.282	0.392	–0.110	
28 ps	0.342	0.508	–0.838	
Long lived			0.948	
0.68 ns				0.024

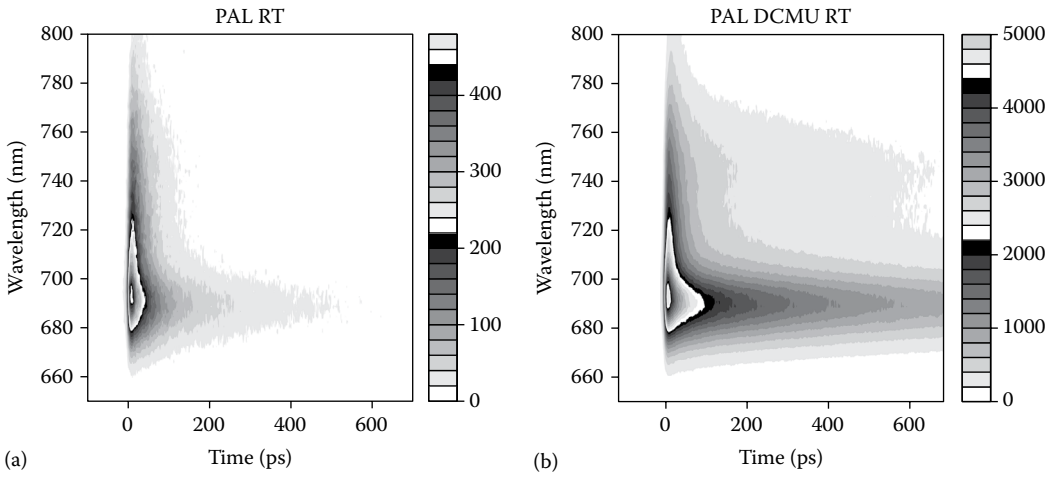

Figure 20.5 Filled contour plot of the time-resolved emission spectrum of PAL cells (that contain both PSI and PSII) at room temperature after 400 nm excitation. Time step ≈ 0.8 ps, wavelength step ≈ 2 nm. **(a)** PSIIRC in the open state, **(b)** PSIIRC in the closed state due to the presence of DCMU.

20.5.1 Global analysis of PAL with PSIIRC in the open state

Four components are sufficient to describe the data. The estimated lifetimes (reciprocals of estimated rate constants k_i) are 4.6 ± 0.2, 16.5 ± 0.3, 45.8 ± 0.5, and 382 ± 3 ps. Judging the DAS is less straightforward than with BE. The fastest lifetime (4.6 ps) again corresponds to equilibration in PSI, where the rise of the Red Chl *a* is evidenced by the negative amplitudes above 690 nm. The other three DAS are all positive and demonstrate photochemical quenching on three time scales. Apparently, both PSI and PSII show quenching on time scales of 16 and 46 ps. The final lifetime of 382 ps can safely be assigned to PSII. The EAS confirm this rough picture. However, target analysis is mandatory to disentangle the contributions of PSI and PSII. From the SVD of the data (not shown), it is clear that three temporally and spectrally different components are present. The fourth pair of left and right singular vectors represents noise. Thus, it can be concluded that in these data, the PSII dynamics are describable with a single spectrum decaying multiexponentially (Figure 20.6).

20.5.2 Simultaneous target analysis of both PAL data sets

Although a target analysis of each individual PAL data set is feasible, it is more instructive to present here a simultaneous analysis in order to demonstrate that both PAL data sets can be described by a single model that differs only in the parameters describing the open or closed condition of the PSIIRC (Figure 20.7).

Now, there are three K matrices. The eigenvalues of the PSI K matrix correspond to lifetimes of 3.7 and 26.6 ps. These lifetimes are slightly shorter than those estimated in the BE target analysis. The estimated PSI SAS of the BE and PAL mutants are practically identical, apart from a small shift due to wavelength calibration uncertainty. Hence, the PSI results of the PAL mutant will not be discussed further. The relative contributions of PSI and PSII can be estimated. Assuming that PSI is in trimeric form and PSII in dimeric form, they contain $3 \times 96 = 288$ and $2 \times 35 = 70$ Chl *a*, respectively. We then estimate a stoichiometry of 1.74 or 1.83 PSII dimer per PSI trimer for the samples with PSIIRC in the open or closed condition, respectively. When expressed as the ratio of PSIRC to PSIIRC, this corresponds to 0.86 or 0.82, which is in agreement with the values reported by Stadnichuk et al. (2009) of 0.7 ± 0.2 and 0.76 (Krumova et al. 2010; Tian et al. 2013).

Finally, the amplitude matrices A describing the PSII dynamics with PSIIRC in the open or closed condition are presented in Tables 20.2 and 20.3, respectively. The interpretation of the amplitude matrix is as follows (neglecting the IRF): $c_{B2,open} = 0.226 \exp(-t/55) + 0.071 \exp(-t/417)$, $c_{B2,closed} = 0.108 \exp(-t/123) + 0.200 \exp(-t/877)$.

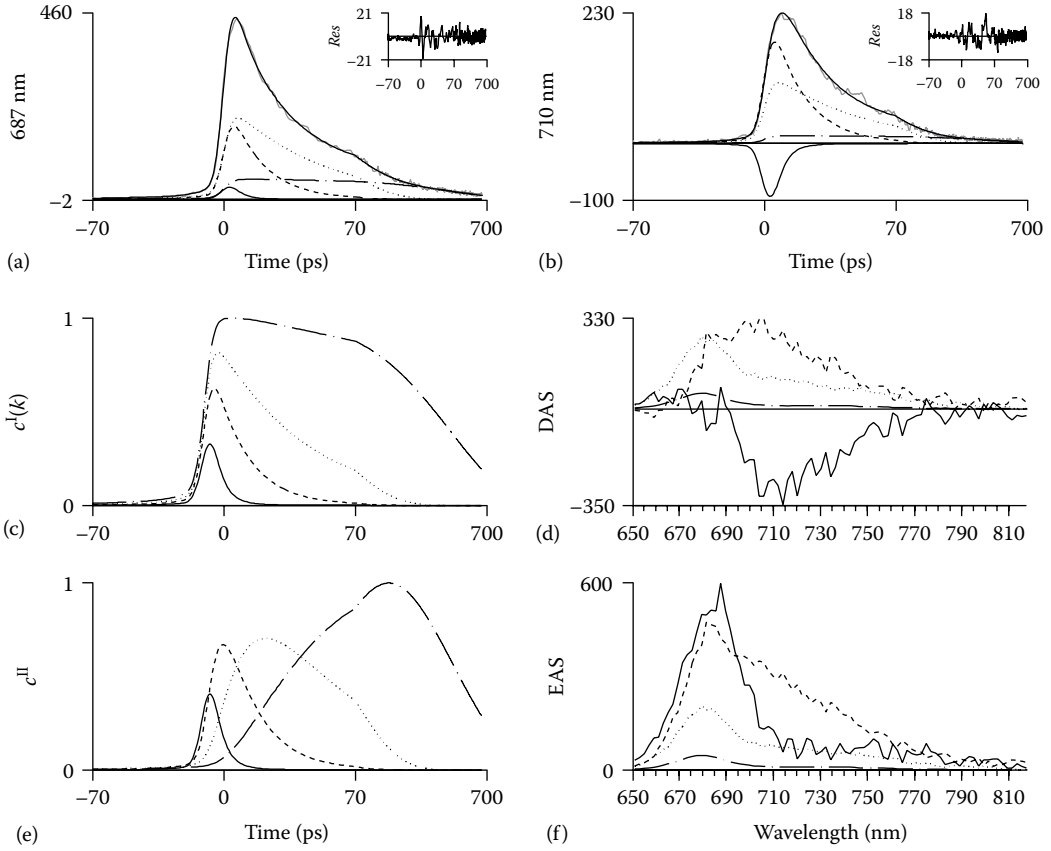

Figure 20.6 Results from global analysis of PAL mutant data with PSIIRC in the open state depicted in Figure 20.5a. Note that in a–c and e, the time axis is linear from –70 to +70 ps relative to the maximum of the IRF and logarithmic thereafter. Insets in a and b show residuals. **(a)** Data (in grey) and fit (in black) of 687 nm emission trace showing multiexponential decay. Contributions of the four exponential decays with different lifetimes (shown in c) multiplied by their amplitudes at 687 or 710 nm (shown in d) are indicated by line type in panels a and b. **(b)** Data (in grey) and fit (in black) of 710 nm emission trace showing multiexponential rise (visible as a contribution of $c^{I}(k_1)$ with negative amplitude) and decay. **(c)** Exponential decays $c^{I}(k_l)$. Estimated lifetimes (in panels c and e): 4.6 ps (solid), 16.5 ps (dashed), 45.8 ps (dotted), and 382 ps (dot-dashed). **(d)** Estimated Decay-Associated Spectra (DAS). **(e)** Evolutionary concentration profiles c_l^{II} (assuming a sequential kinetic scheme with increasing lifetimes). **(f)** Estimated Evolution-Associated Spectra (EAS).

Effectively, in PSII cores two lifetimes are sufficient to describe photochemical quenching *in vivo* in the PAL mutant. *In vitro*, two additional short lifetimes (<10 ps) with small contributions can be resolved from time-resolved emission spectra of PSII cores of *Thermosynechococcus elongatus* with open PSIIRC (Miloslavina et al. 2006; van der Weij–de Wit et al. 2011). The *in vitro* PSII core emission from van der Weij–de Wit et al. (2011) can be well fitted with the simple two-compartment scheme of bulk and radical pair, resulting in $c_{B2,open}^{in\,vitro} = 0.834\exp(-t/42) + 0.156\exp(-t/173)$. The photochemical quenching parameters of PSII are collated in Table 20.4.

Thus, the main differences with open RC are that *in vivo* photochemical quenching is a bit slower than *in vitro* and that the free energy difference between B2 and RP2 is smaller. The transmembrane potential could be the cause thereof. *In vivo* with closed RC, the negative charge on Q_A^- lifts the RP2 to a higher free energy than that of B2.

Since it is not possible to resolve the small contributions of the faster equilibration lifetimes (<10 ps), no attempt is made to resolve the equilibration

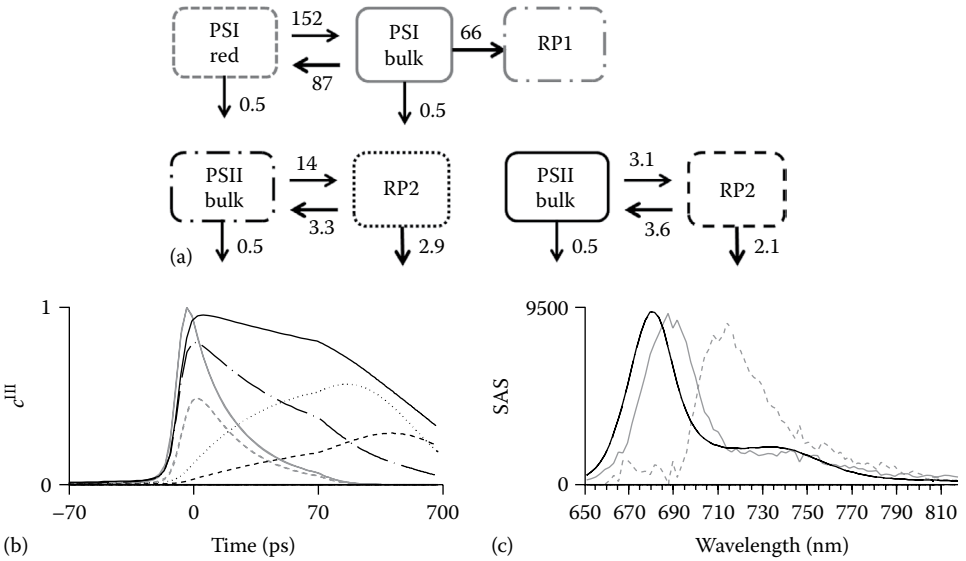

Figure 20.7 **(a)** Kinetic scheme used for the target analysis of the PAL data depicted in Figure 20.5. After excitation in the Soret band, three compartments are populated: Bulk Chl *a* (B1), Red Chl *a* (R1) of PSI, and Bulk Chl *a* (B2) of PSII. B2 equilibrates with a nonradiative radical pair (RP2) compartment, thus effectively describing the biexponential decay of the PSII emission. Excitations are trapped from B1 or B2. Rates in 1/ns. **(b)** Concentration profiles c_j^{III}; note that the time axis is linear from –70 to +70 ps relative to the maximum of the IRF and logarithmic thereafter. **(c)** Species-Associated Spectra (SAS). Key in a, b, and c: PSI in grey with B1 (solid), R1 (dashed), PSII in black with (in the closed state) B2 (solid), RP2 (dashed), and (in the open state) B2 (dot-dashed), RP2 (dotted).

Table 20.2 Amplitude matrix for the different lifetimes of the PAL data with open PSIIRC describing PSII

Compartment	B2	RP2
Excitation	0.297	0
55 ps	0.226	−0.262
417 ps	0.071	0.262

Table 20.3 Amplitude matrix for the different lifetimes of the PAL data with closed PSIIRC describing PSII

Compartment	B2	RP2
Excitation	0.308	0
123 ps	0.108	−0.137
877 ps	0.200	0.137

within the B2 compartment between the PSIIRC and the CP43 and CP47 antenna complexes, which is still disputed (Barter et al. 2001; Miloslavina et al. 2006; Raszewski and Renger 2008; van der Weij–de Wit et al. 2011; Tian et al. 2013).

Table 20.4 Estimated photochemical quenching parameters of PSII, rates in 1/ns, $\Delta G_{B2,RP2}$ in meV

Sample	$k_{B2\rightarrow RP2}$	$k_{RP2\rightarrow B2}$	$k_{RP2\rightarrow}$	$\Delta G_{B2,RP2}$
In vitro, open	20	2.1	6.5	57
In vivo, open	14	3.3	2.9	37
In vivo, closed	3.1	3.6	2.1	−4

20.6 CONCLUSIONS

Systems biophysics can resolve *in vivo* processes. Combined with knowledge from the literature, simultaneous analysis of different experiments can describe the functioning of complex photosynthetic systems. The high time resolution experiments of *in vitro* systems, preferably with selective excitation of, for example, the RC (Groot et al. 2005; Holzwarth et al. 2006; Muller et al. 2010) can reveal details of ultrafast processes that are obscured by the relatively slow dynamics of energy transfer to

the RC. Cyanobacteria are promising model systems for a full description of the intact thylakoid membrane with the help of target analysis.

ACKNOWLEDGMENTS

The data analyzed have been expertly measured by Lijin Tian under the supervision of Herbert van Amerongen in the Laboratory of Biophysics of Wageningen University. Joris Snellenburg is thanked for critically reading the text. This project was partly carried out within the research program of BioSolar Cells, cofinanced by the Dutch Ministry of Economic Affairs, Agriculture and Innovation. Financial support of the European Research Council is acknowledged (Advanced Grant proposal 267333 PHOTPROT to Rienk van Grondelle).

REFERENCES

Ajlani G, Vernotte C (1998) Construction and characterization of a phycobiliprotein-less mutant of *Synechocystis* sp. PCC 6803. *Plant Molecular Biology* 37 (3):577–580.

Arcioni A, Zannoni C (1984) Intensity deconvolution in fluorescence depolarization studies of liquids, liquid-crystals and membranes. *Chemical Physics* 88 (1):113–128.

Barter LMC, Bianchietti M, Jeans C, Schilstra MJ, Hankamer B, Diner BA, Barber J, Durrant JR, Klug DR (2001) Relationship between excitation energy transfer, trapping, and antenna size in photosystem II. *Biochemistry* 40 (13):4026–4034.

Beechem JM (1989) A 2nd generation global analysis program for the recovery of complex inhomogeneous fluorescence decay kinetics. *Chemistry and Physics of Lipids* 50 (3–4):237–251.

Beechem JM, Ameloot M, Brand L (1985) Global and target analysis of complex decay phenomena. *Analytical Instrumentation* 14 (3–4):379–402.

Chukhutsina V, Tian L, Ajlani G, van Amerongen H (2013) Time-resolved fluorescence of photosystem I in vivo: Global and target analysis. In: Kuang T, Lu C, Zhang L (eds.) *Photosynthesis Research for Food, Fuel and Future: 15th International Conference on Photosynthesis*, Beijing, China, Symposium 16 Photoprotection, Photoinhibition and Dynamics. Springer, Heidelberg, Germany, pp. 465–468.

Croce R, van Amerongen H (2013) Light-harvesting in photosystem I. *Photosynthesis Research* 116 (2–3):153–166.

Gobets B, van Stokkum IHM, Rogner M, Kruip J, Schlodder E, Karapetyan NV, Dekker JP, van Grondelle R (2001) Time-resolved fluorescence emission measurements of photosystem I particles of various cyanobacteria: A unified compartmental model. *Biophysical Journal* 81 (1):407–424.

Golub G, Pereyra V (2003) Separable nonlinear least squares: The variable projection method and its applications. *Inverse Problems* 19 (2):R1–R26.

Golub GH, LeVeque RJ (1979) Extensions and uses of the variable projection algorithm for solving nonlinear least squares problems. *Proceedings of the 1979 Army Numerical Analysis and Computers Conference*, White Sands Missile Range, NM, ARO Report 79-3.

Golub GH, Pereyra V (1973) Differentiation of pseudo-inverses and nonlinear least-squares problems whose variables separate. *SIAM Journal on Numerical Analysis* 10 (2):413–432.

Golub GH, Van Loan CF (1996) *Matrix Computations*. The Johns Hopkins University Press, Baltimore, MD.

Groot ML, Pawlowicz NP, van Wilderen L, Breton J, van Stokkum IHM, van Grondelle R (2005) Initial electron donor and acceptor in isolated Photosystem II reaction centers identified with femtosecond mid-IR spectroscopy. *Proceedings of the National Academy of Sciences of the United States of America* 102 (37):13087–13092.

Hendler RW, Shrager RI (1994) Deconvolutions based on singular-value decomposition and the pseudoinverse—A guide for beginners. *Journal of Biochemical and Biophysical Methods* 28 (1):1–33.

Henry ER, Hofrichter J (1992) Singular value decomposition—Application to analysis of experimental-data. *Methods in Enzymology* 210:129–192.

Holzwarth AR (1996) Data analysis of time-resolved measurements. In: Amesz J, Hoff AJ (eds.) *Biophysical Techniques in Photosynthesis*. Kluwer, Dordrecht, the Netherlands, pp. 75–92.

Holzwarth AR, Muller MG, Reus M, Nowaczyk M, Sander J, Rogner M (2006) Kinetics and mechanism of electron transfer in intact photosystem II and in the isolated reaction center: Pheophytin is the primary electron acceptor. *Proceedings of the National Academy of Sciences of the United States of America* 103 (18):6895–6900.

Krumova SB, Laptenok SP, Borst JW, Ughy B, Gombos Z, Ajlani G, van Amerongen H (2010) Monitoring photosynthesis in individual cells of *Synechocystis* sp. PCC 6803 on a picosecond timescale. *Biophysical Journal* 99 (6):2006–2015.

Miloslavina Y, Szczepaniak M, Muller MG, Sander J, Nowaczyk M, Rogner M, Holzwarth AR (2006) Charge separation kinetics in intact photosystem II core particles is trap-limited. A picosecond fluorescence study. *Biochemistry* 45 (7):2436–2442.

Mullen KM, van Stokkum IHM (2007) TIMP: An R package for modeling multi-way spectroscopic measurements. *Journal of Statistical Software* 18 (3):1–46.

Mullen KM, van Stokkum IHM (2009) The variable projection algorithm in time-resolved spectroscopy, microscopy and mass spectrometry applications. *Numerical Algorithms* 51 (3):319–340.

Muller MG, Griebenow K, Holzwarth AR (1992) Primary processes in isolated bacterial reaction centers from *Rhodobacter-sphaeroides* studied by picosecond fluorescence kinetics. *Chemical Physics Letters* 199 (5):465–469.

Muller MG, Hucke M, Reus M, Holzwarth AR (1996) Annihilation processes in the isolated D1-D2-cyt-b559 reaction center complex of photosystem II. An intensity-dependence study of femtosecond transient absorption. *Journal of Physical Chemistry* 100 (22):9537–9544.

Muller MG, Slavov C, Luthra R, Redding KE, Holzwarth AR (2010) Independent initiation of primary electron transfer in the two branches of the photosystem I reaction center. *Proceedings of the National Academy of Sciences of the United States of America* 107 (9):4123–4128.

Nagle JF (1991) Solving complex photocycle kinetics—Theory and direct method. *Biophysical Journal* 59 (2):476–487.

Nagle JF, Parodi LA, Lozier RH (1982) Procedure for testing kinetic-models of the photocycle of Bacteriorhodopsin. *Biophysical Journal* 38 (2):161–174.

Peterman EJG, Wenk SO, Pullerits T, Palsson LO, van Grondelle R, Dekker JP, Rogner M, van Amerongen H (1998) Fluorescence and absorption spectroscopy of the weakly fluorescent chlorophyll a in cytochrome b(6)f of *Synechocystis PCC6803*. *Biophysical Journal* 75 (1):389–398.

Raszewski G, Renger T (2008) Light harvesting in photosystem II core complexes is limited by the transfer to the trap: Can the core complex turn into a photoprotective mode? *Journal of the American Chemical Society* 130 (13):4431–4446.

Shrager RI (1986) Chemical-transitions measured by spectra and resolved using singular value decomposition. *Chemometrics and Intelligent Laboratory Systems* 1 (1):59–70.

Snellenburg JJ, Dekker JP, van Grondelle R, van Stokkum IHM (2013) Functional compartmental modeling of the photosystems in the thylakoid membrane at 77 K. *The Journal of Physical Chemistry B* 117 (38):11363–11371.

Snellenburg JJ, Laptenok SP, Seger R, Mullen KM, van Stokkum IHM (2012) Glotaran: A Java-based graphical user interface for the R-package TIMP. *Journal of Statistical Software* 49(3):1–22.

Stadnichuk IN, Lukashev EP, Elanskaya IV (2009) Fluorescence changes accompanying short-term light adaptations in photosystem I and photosystem II of the cyanobacterium *Synechocystis* sp PCC 6803 and phycobiliprotein-impaired mutants: State 1/State 2 transitions and carotenoid-induced quenching of phycobilisomes. *Photosynthesis Research* 99 (3):227–241.

Tian L, Farooq S, van Amerongen H (2013) Probing the picosecond kinetics of the photosystem II core complex in vivo. *Physical Chemistry Chemical Physics* 15 (9):3146–3154.

van Amerongen H, Croce R (2013) Light harvesting in photosystem II. *Photosynthesis Research* 116 (2–3):251–263.

van der Weij–de Wit CD, Dekker JP, van Grondelle R, van Stokkum IHM (2011) Charge separation is virtually irreversible in photosystem II core complexes with oxidized primary quinone acceptor. *The Journal of Physical Chemistry A* 115 (16):3947–3956.

van Grondelle R, Dekker JP, Gillbro T, Sundström V (1994) Energy-transfer and trapping in photosynthesis. *Biochimica et Biophysica Acta* 1187 (1):1–65.

van Stokkum IHM (2005) Global and target analysis of time-resolved spectra. Lecture Notes for the Troisième Cycle de la Physique en Suisse Romande. Department of Physics and Astronomy, Vrije Universiteit, Amsterdam, the Netherlands.

van Stokkum IHM, Bal HE (2006) A problem solving environment for interactive modelling of multiway data. *Concurrency and Computation: Practice and Experience* 18:263–269.

van Stokkum IHM, Desquilbet TE, van der Weij-de Wit CD, Snellenburg JJ, van Grondelle R, Thomas J-C, Dekker JP, Robert B (2013) Energy transfer and trapping in red-chlorophyll-free photosystem I from *Synechococcus* WH 7803. *The Journal of Physical Chemistry B* 117 (38):11176–11183.

van Stokkum IHM, Larsen DS, van Grondelle R (2004) Global and target analysis of time-resolved spectra. *Biochimica et Biophysica Acta* 1657:82–104.

van Stokkum IHM, van Oort B, van Mourik F, Gobets B, van Amerongen H (2008) (Sub)-Picosecond spectral evolution of fluorescence studied with a synchroscan streak-camera system and target analysis. In: Aartsma TJ, Matysik J (eds.) *Biophysical Techniques in Photosynthesis*, vol. II. Advances in Photosynthesis and Respiration, vol. 26. Springer, Dordrecht, the Netherlands, pp. 223–240.